Dynamic strength and ductility of ultra-high performance concrete with flow-induced fiber alignment

Andrew B. Groeneveld[a,b,*], Theresa M. Ahlborn[a], C. Kennan Crane[b], Charles A. Burchfield[b], Eric N. Landis[c]

[a] Michigan Technological University, Department of Civil and Environmental Engineering, 1400 Townsend Drive, Houghton, MI 49931-1295, USA
[b] U.S. Army Engineer Research and Development Center, ATTN: CEERD-GSS, 3909 Halls Ferry Road, Vicksburg, MS 39180-6199, USA
[c] University of Maine, Department of Civil and Environmental Engineering, Orono, ME 04469-5711, USA

A R T I C L E   I N F O

A B S T R A C T

The effect of fiber alignment on dynamic strength and ductility of an ultra-high performance concrete has been investigated. A beam was cast to produce a realistic level of flow-induced fiber alignment. Cores were drilled from the beam, and fiber orientation was non-destructively characterized using x-ray computed tomography. Fiber orientations in three orthogonal directions were significantly different at a 95% confidence level, with fibers preferentially aligned in the direction of flow during placement. Cored specimens were then tested in high-strain rate compression using a split-Hopkinson pressure bar. Dynamic compressive strength was independent of fiber orientation for the specimens tested. Ductility, measured by the strain at peak stress, increased with the proportion of fibers oriented perpendicular to the applied load.

Published by Elsevier Ltd.

1. Introduction

Ultra-high performance concrete (UHPC) can use fiber reinforcement to increase tensile strength and control cracks. When casting structural elements with fiber-reinforced UHPC, fibers tend to align. Factors affecting alignment include flow of the concrete, use of vibration for consolidation, and wall effects from the formwork [1]. Fiber alignment results in strength anisotropy [2,3], which needs to be accounted for in design. Assuming that fibers are randomly oriented may be unconservative. In previous dynamic tests on UHPC, post-failure inspection indicated that some failures occurred on weak planes where there were few fibers [4]. This work examines the fiber orientation that occurs in a cast UHPC beam, and the effect this orientation has on dynamic compressive strength and ductility.

The split-Hopkinson pressure bar (SHPB) is used to conduct high-strain rate material tests. Developed by Kolsky [5], this technique places a specimen between two long, elastic bars. These bars are instrumented to measure the propagation of stress waves, from which the specimen's response can be determined. A schematic of an SHPB is shown in Fig. 1. An elastic compressive stress wave is produced in the input bar by the impact of a striker rod, typically fired from a compressed-gas cannon. When testing brittle materials, a pulse shaper can be placed on the face of the input bar. The pulse shaper deforms during impact, resulting in a stress wave with a tapered rise [6]. The stress wave propagates along the input bar until reaching the input bar-specimen interface. When the specimen has a lower acoustic impedance than the bar, part of the wave is reflected back into the input bar as a tensile stress wave. The rest of the wave continues into the specimen and is then transmitted into the output bar. This description has ignored wave reflections in the specimen, which must be considered when assessing the uniformity of stress [7].

Data are usually analyzed under the assumptions that wave propagation in the bars can be adequately described by the one-dimensional elastic theory, stress in the specimen is uniform, and the effects of friction and inertia are negligible [7]. Then, the specimen engineering stress (σ_s), engineering strain (ε_s), and engineering strain rate ($\dot{\varepsilon}_s$) can be determined as

$$\sigma_s(t) = \frac{A_b E_b}{2A_s}(\varepsilon_I(t) + \varepsilon_R(t) + \varepsilon_T(t)), \tag{1}$$

$$\varepsilon_s(t) = \int_0^t \dot{\varepsilon}_s(\tau)\, d\tau, \tag{2}$$

* Corresponding author. Present address: U.S. Army Engineer Research and Development Center, ATTN: CEERD-GSS, 3909 Halls Ferry Road, Vicksburg, MS 39180-6199, USA.
E-mail address: andrew.b.groeneveld@usace.army.mil (A.B. Groeneveld), tess@mtu.edu (T.M. Ahlborn), charles.k.crane@usace.army.mil (C.K. Crane), charles.a.burchfield@usace.army.mil (C.A. Burchfield), landis@maine.edu (E.N. Landis).
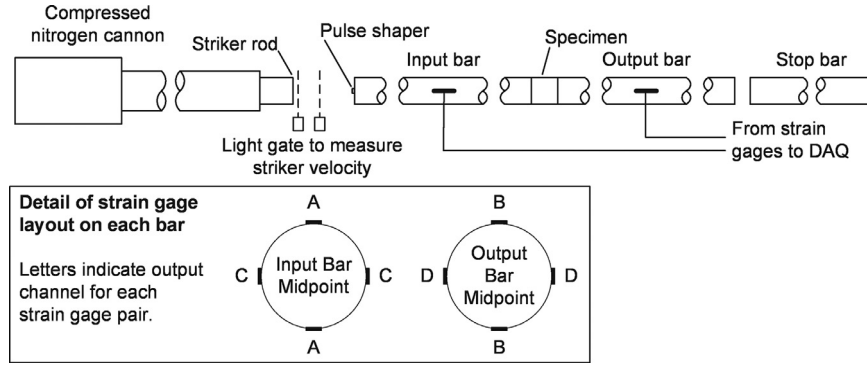
Fig. 1. Schematic of the SHPB.

$$\dot{\varepsilon}_s(t) = \frac{c_{0,b}}{L_s}(\varepsilon_I(t) - \varepsilon_R(t) - \varepsilon_T(t)), \tag{3}$$

where A is cross-sectional area, E is the elastic modulus, $c_0 = (E/\rho)^{1/2}$ is the thin-rod elastic wave speed, ρ is mass density, L is length, and the subscripts b and s refer to the bar and specimen, respectively. Note that stresses and strains are taken as positive in compression throughout this article. The measured strains ε_I, ε_R, and ε_T correspond to the incident, reflected, and transmitted stress waves, respectively. These strains are measured by strain gages bonded to the bars at their midpoints. An example of the strain gage output is shown in Fig. 2.

Cor-Tuf Baseline, a UHPC developed by the U.S. Army Corps of Engineers [8], has been tested in both unconfined [4] and confined [9] dynamic compression using an SHPB. Cor-Tuf Baseline is rate-sensitive, achieving higher strengths at increasing rates of loading. This strength increase is typically quantified using the dynamic increase factor (DIF), which is the ratio of dynamic strength to the corresponding quasi-static strength. The reduced time for micro-crack propagation at high strain rates is thought to be responsible for strengthening [10]. However, it is also known that confinement in dynamic tests increases the measured strength [10,11]. When an axial compressive load is rapidly applied, a test specimen's radial expansion due to the Poisson effect is opposed by inertia forces. This is equivalent to applying a radial confining stress, which has been determined under the assumption of linear elasticity by Forrestal et al. [12]. However, concrete is a non-linear material. Also, the contribution of inertial confinement to the strength increase in high-strain rate tests can only be assessed indirectly, as the effect of inertia cannot be eliminated. A number of studies (for example,

[13−15]) have used numerical simulation to study the effects of inertial confinement on SHPB tests of concrete.

Fibers are most efficient in crack-bridging when oriented perpendicular to a crack. Therefore, when a material is loaded in tension, fibers should be oriented parallel to the tensile stress [16]. Similarly, when a material is loaded in compression, fibers should generally be oriented perpendicular to the compressive stress [2,3].

Fiber orientation can be described using the orientation number, typically η. Traditionally, η has been determined by cutting a cross-section in a specimen and examining the fibers in the cut surface. In this case, η is the ratio of the projected fiber length normal to the surface to the total fiber length [17]. In light of the different effects of orientation in tension and compression, the orientation number can be generalized as follows:

$$\eta_\parallel = \frac{1}{N}\sum_{i=1}^{N}\cos(\theta_i), \tag{4}$$

$$\eta_\perp = \frac{1}{N}\sum_{i=1}^{N}\sin(\theta_i), \tag{5}$$

where N is the total number of fibers, and θ_i is the angle that the ith fiber makes with the axis of loading. The parallel orientation number, $\eta_\parallel$, is the fraction of fiber length that is projected parallel to the applied load. Similarly, the perpendicular orientation number, $\eta_\perp$, is the fraction of fiber length that is projected perpendicular to the applied load. Although this definition suggests a simple geometric relationship between the two orientation numbers, it is generally *not* the case that $\eta_\parallel^2 + \eta_\perp^2 = 1$. This would hold for a single fiber, but
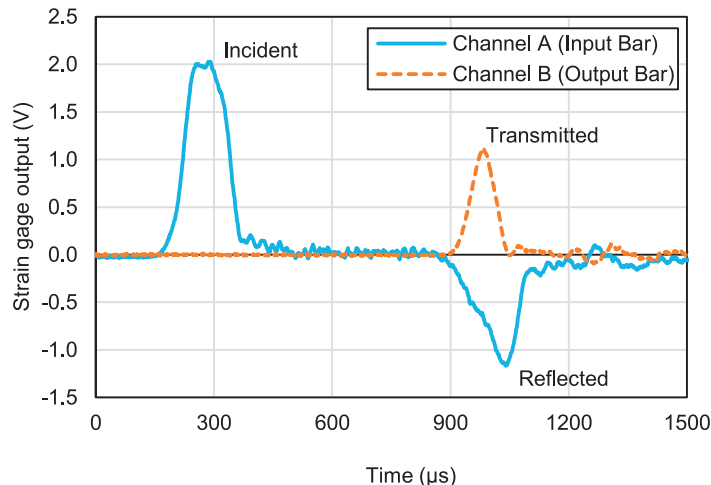

Fig. 2. Strain gage output from test of specimen X–D–2M.

Table 1
Cor-Tuf Baseline mixture proportions.

Material	Weight fraction
Class H cement (Quality Stone and Readymix)	1.000
Silica fume (Elkem, ES900W)	0.390
Sil co Sil (U.S. Silica)	0.277
Silica sand (U.S. Silica, F-50)	0.970
Steel fibers (Bekaert, Dramix ZP 305)	0.314
Superplasticizer (W.R. Grace, ADVA 190)	0.017
Water (Vicksburg, MS, municipal supply)	0.211

the relationship breaks down when an average is taken over many fibers.

There are a number of methods for determining fiber orientation, which can be broadly classified as destructive or non-destructive. Destructive methods typically involve cutting a section in a specimen and counting fiber density per unit area [17,18] or measuring the dimensions of fiber cross-sections [19]. Although destructive methods are simple, the advantage of non-destructive testing is that both fiber orientation and mechanical properties can be determined for the same specimen. This allows correlations between the two to be sought. A variety of non-destructive approaches based on electrical conductivity have been developed [20–23]. However, these can only determine an average orientation within the specimen. To obtain information on individual fibers, methods such as x-ray computed tomography (CT) must be used. X-ray CT works by taking radiographs (also called projections) of a specimen from many different angles [24]. At each pixel in a radiograph, the intensity is determined by the attenuation of all the material that the x-ray travelled through. When radiographs are taken from many angles, the attenuation at each point within the specimen can be reconstructed. The theoretical basis for this process is due to Radon [25]; modern reconstruction algorithms include filtered backprojection (FBP) and direct Fourier inversion (DFI) [24].

2. Material and methods

2.1. Specimen preparation

The largest aggregate in Cor-Tuf Baseline is a silica sand with a diameter of about 0.6 mm (0.024 in.), and the water-to-cementitious materials ratio is around 0.15 [8]. Internal reinforcement is provided by steel fibers; 0.55-mm (0.022-in.) diameter, 30-mm (1.2-in.) long hooked-end fibers are typically used, although other fiber types have been investigated [26]. Mixture proportions for Cor-Tuf Baseline UHPC are given in Table 1. Fiber reinforcement is 3.15% by volume. Note that the manufacturer now uses the designation 3D 55/30 BG for the Dramix ZP 305 fibers [26]. Tests on

three 100×200-mm (4×8-in.) cylinders gave a 28-day compressive strength of 190 MPa (27.5 ksi).

A beam measuring roughly 200-mm wide, 610-mm high, and 3050-mm long (8-in. wide, 24-in. high, and 10-ft long) was constructed as a representative structural element. In keeping with typical practice, the beam was cast from one end, and concrete was allowed to flow and fill the formwork. Vibration was applied to the form walls, but not to the concrete itself, to achieve reasonable consolidation without fiber segregation. The narrow beam was intended to give a realistic assessment of fiber alignment due to flow. The beam received 7 days of moist curing followed by 7 days of steam curing. To avoid possible thermal cracking, the beam was cooled gradually over 4 days following steam treatment.

For easier handling, the beam was then cut into 8 blocks using a gantry saw (Sawing Systems Model 521C). Fig. 3 shows the overall layout of the beam and defines the coordinate directions used in the rest of this article. The x-axis is the beam's longitudinal axis and is positive in the direction of flow. The y-axis is vertical and positive upwards, and the z-axis extends through the beam's web with its positive direction determined by the right-hand rule. To allow cores to be drilled in multiple directions, the blocks were further divided into smaller prisms. Cuts to make prisms are shown in Fig. 3 using solid lines, and the locations of cores are shown in dashed lines. Cores were drilled using 76-mm (3-in.) diameter core barrels and were cut to 76-mm (3-in.) lengths for dynamic compression testing. Because of the length of the fibers (30 mm), fairly large specimens were used to better represent the bulk material. The current specimens have dimensions that are 2.5 times the fiber length. A number of quasi-static test specimens were also produced for a separate test series. Finally, the ends of specimens were ground to be parallel within a 0.5-degree tolerance.

2.2. Fiber orientation determination

The internal structure of specimens was imaged using x-ray CT scans performed in the Advanced Materials Characterization Laboratory (AMCL) at the University of Florida. A North Star Imaging, Inc., model SR-450 with a 225-kV microfocus x-ray source was used to scan specimens. The manufacturer's software efx-CT was used to reconstruct 3D images of the specimens from the captured radiographs. A slice through the reconstruction of specimen X-D-2 M is shown in Fig. 4. Voxel sizes in the reconstructed images ranged from 39 μm to 42 μm. Image processing techniques were then used to compute fiber orientation vectors. The algorithm used was developed by Trainor et al. [27]; in the current research, modifications by Oesch [28] were also incorporated. Full details on the CT scanning and image processing procedure may be found in Groeneveld [29].
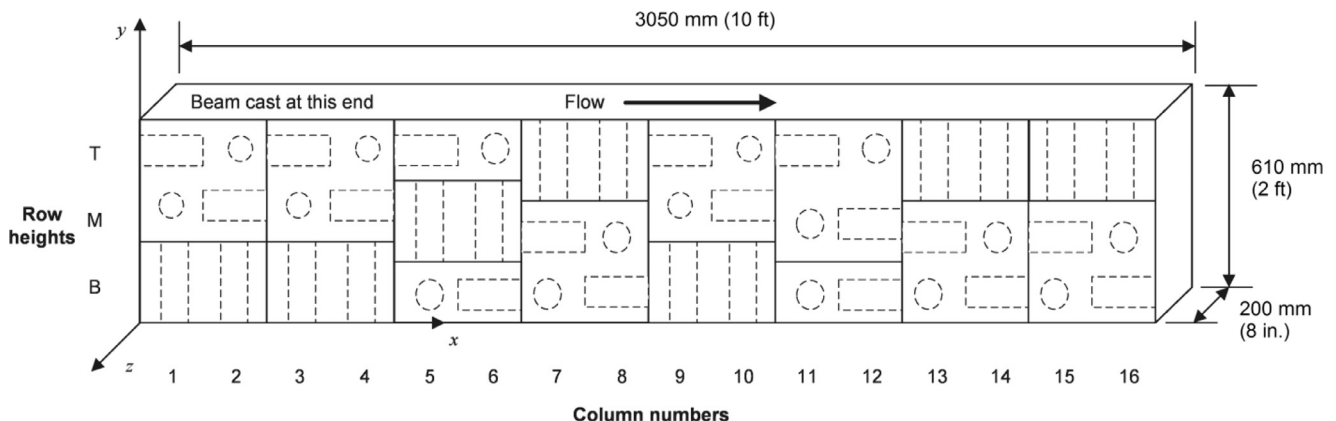

Fig. 3. Schematic view of beam. Cores are shown with dashed lines; cuts for blocks or prisms are shown with solid lines. Not to scale.
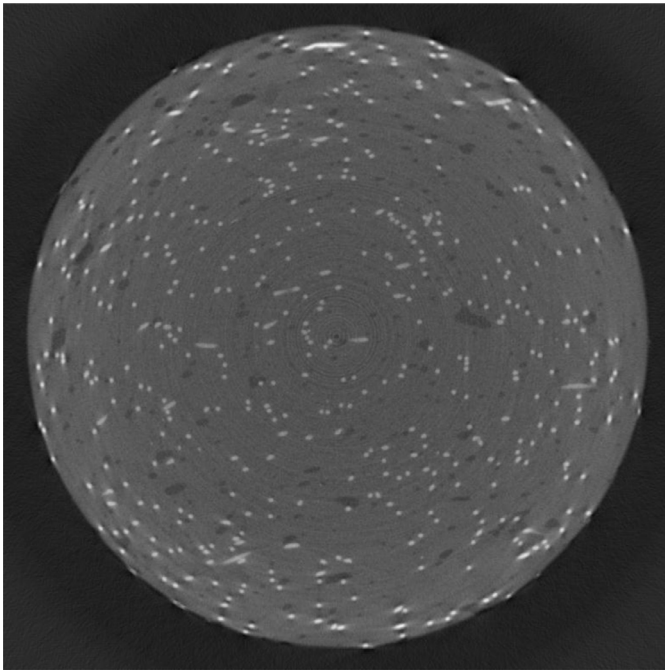
Fig. 4. Slice through reconstructed 3D image of specimen X-D-2M. In the image, brightness indicates x-ray attenuation, with the steel fibers appearing in white.

2.3. Dynamic compression testing

Dynamic compression testing was performed using a 76-mm (3-in.) diameter SHPB at Michigan Technological University. All bars are made of 1045S steel with a tensile strength of roughly 640 MPa (92 ksi). The input and output bars are 3660-mm (12-ft) long. A 305-mm (12-in.) long striker bar was used for all tests. The striker was launched from a compressed nitrogen cannon using a pressure of 550 kPa (80 psi). A C1100 copper pulse shaper, measuring 19 mm (0.75 in.) in diameter and 2.2-mm (0.085-in.) thick, was affixed to the input bar using a thin layer of white lithium grease. A thin layer of dry film lubricant (Liquid Wrench Dry Lubricant) was applied to the ends of the input and output bars before placing the specimen.

Two pairs of strain gages (Vishay Micro-Measurements EA-06-125AC-350) were bonded to the midpoints of the input and output bars as shown in Fig. 1. Each pair was connected to a BAM-1 unit (Vishay or Ellis Associates) which connects the strain gages in a half-Wheatstone bridge to cancel any bending effects [30]. The BAM-1 unit preamplifies the output voltage from the Wheatstone bridge; this amplified signal is read by a Picoscope 4424 digital oscilloscope (Pico Technology). Specimen response was calculated using Eqs. (1)–(3), taking the average of results from the A/B and C/D channels.

High-speed video of tests was captured using a Phantom 7.1 camera at roughly 26,000 frames/s with a 2-μs exposure for each frame. To improve the visibility of cracks, a thin coat of flat white enamel spraypaint was applied to the specimens.

3. Results and discussion

3.1. Fiber orientation in the beam

Of the 18 specimen scans collected, 2 had artifacts that made fiber orientation calculations impossible. Therefore, orientation results are only given for 16 specimens. All 18 specimens were tested in dynamic compression. Values of the perpendicular orientation number ($\eta_\perp$) for specimens cored in the x-, y-, and z-directions are shown in Fig. 5. The mean perpendicular orientation number was 0.558 for the x-axis (6 specimens), 0.931 for the y-axis

(5 specimens), and 0.843 for the z-axis (5 specimens). Values of $\eta_\perp$ for specimens cored in each direction were compared using the Games-Howell simultaneous test [31] implemented in Minitab 17 Statistical Software [32]. Results of the test are summarized in Table 2. Note that, for a specimen cored in the x-axis, the axis of loading will also be the x-axis, and so on. A 95% confidence interval (CI) is given for the difference between the mean for each direction. If the 95% CI does not contain zero, the difference is significant at a 95% confidence level. It was found that specimens in each direction had statistically significantly different perpendicular orientation numbers.

Values of the parallel orientation number ($\eta_\parallel$) for specimens cored in the x-, y-, and z-directions are shown in Fig. 6. The mean parallel orientation number was 0.740 for the x-axis (6 specimens), 0.290 for the y-axis (5 specimens), and 0.424 for the z-axis (5 specimens). Values of $\eta_\parallel$ for specimens cored in each direction were compared using the Games-Howell simultaneous test, which is sum-
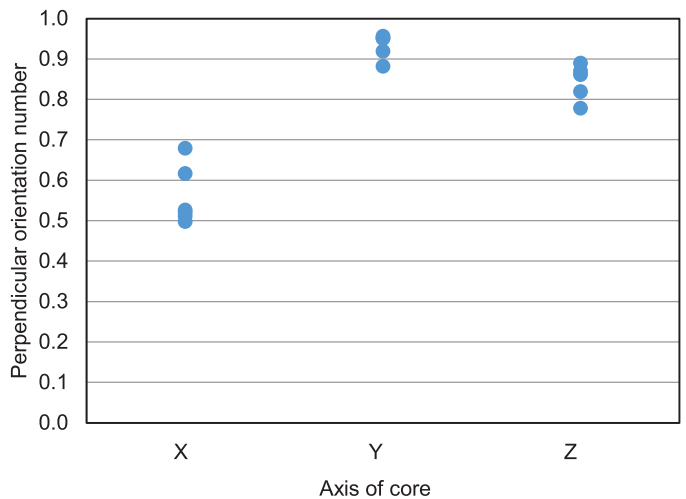

Fig. 5. Perpendicular orientation number, $\eta_\perp$, by core axis.

Table 2
Games-Howell simultaneous test for perpendicular orientation number, $\eta_\perp$.

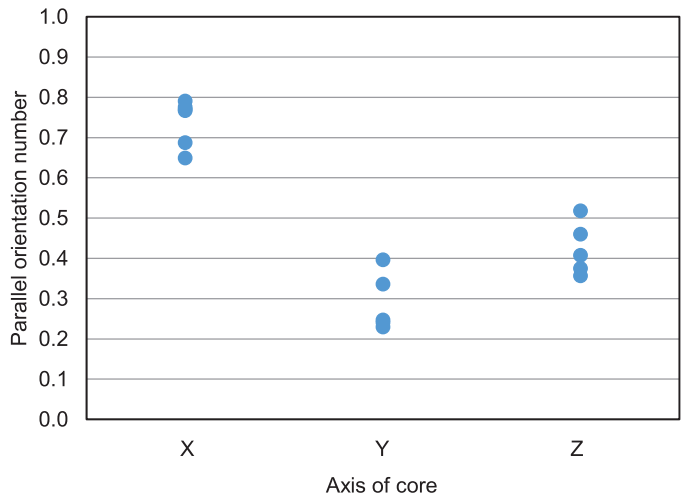| Comparison	Difference of means	95% CI for difference of mean
Y specimens − X specimens	0.373	(0.277, 0.470)
Z specimens − X specimens	0.285	(0.184, 0.386)
Z specimens − Y specimens	−0.088	(−0.160, −0.017)

Fig. 6. Parallel orientation number, $\eta_\parallel$, by core axis.

Table 3
Games-Howell simultaneous test for parallel orientation number, $\eta_\parallel$.

Comparison	Difference of means	95% CI for difference of mean
Y specimens − X specimens	−0.450	(−0.566, −0.334)
Z specimens − X specimens	−0.316	(−0.424, −0.209)
Z specimens − Y specimens	0.134	(0.008, 0.260)

marized in Table 3. Because the CIs do not contain zero, specimens in each direction had significantly different parallel orientation numbers at a 95% confidence level. Thus, the preparation method was effective for making specimens with different orientations.

The fiber orientation in the specimens also gives information about fiber orientation in the beam. The highest values of $\eta_\parallel$ were for the x-direction specimens, indicating that fibers were predominantly aligned in the x-direction, which was the direction of flow. On the other hand, both the y- and z-direction specimens had relatively high values of $\eta_\perp$. This indicates that fibers were mainly perpendicular to the y- and z-axes. This is consistent with fibers aligning in the x-direction. Finally, note that the alignment with the direction of flow was not perfect; $\eta_\parallel = 1$ would indicate that all fibers were oriented in a given direction.

3.2. Dynamic test results

In the SHPB tests, the striker rod velocity prior to impact was 22.6−23.7 m/s (74.1−77.7 ft/s). Strain rates of 130−200 s^{-1} were achieved during testing, and maximum dynamic axial stresses ranged from 263 MPa to 403 MPa (38.1 ksi−58.5 ksi). A dynamic failure is illustrated in Fig. 7, which shows selected frames from high-speed video of an SHPB test. For reference, the input bar is on the right and the output bar is on the left in all images. Frame 1 shows the beginning of cracking, with cracks forming at voids near the output bar side. In frame 2, cracks propagate toward the input bar side. Additional cracks form in frames 3 and 4, with spalling of material in the upper left corner. There is also crushing at the output bar side, which is clearly evident in frame 10. The lower portion of the specimen is beginning to separate and fall away in frame 10. Jumping forward to frame 61, roughly 2.3 ms after cracking started, the lower

fragment has fallen partly out of frame, and the upper, wedge-shaped piece has been launched from the input bar.

Failures were described using the ASTM C39/C39M fracture descriptions [33]. Although these descriptions were developed for quasi-static tests of normal strength concrete without fibers, their standardization makes them useful for these tests as well. Four types of fractures were observed in the tests; examples are shown in Fig. 8. A columnar fracture is shown in Fig. 8a, with cracks running through both ends. A shear fracture is shown in Fig. 8b, where the shear plane crosses from upper right to lower left. Fig. 8c shows a cone-and-split fracture with the cone on the input bar side and cracks extending to the output bar side. The sole example of a side fracture is shown in Fig. 8d. This specimen was intact after testing; although cracks opened, it seems that fibers were effective in bridging the cracks. Columnar fractures were most common, occurring in 12 tests. Definitive statements about the relationship between fracture type and orientation cannot be made based on 18 tests. Orientation does affect the efficiency of fibers in bridging cracks as they form, but crack initiation is also influenced by the location and size of voids and other defects. Characterization of voids, and their effect on crack formation, was outside the scope of this study.

However, it is worth noting that cone-and-split and columnar fractures occurred for specimens cored in all directions, whereas shear fractures did not occur for specimens cored in the z-direction, and side fracture only occurred for a single y-direction specimen.

Dynamic stress-strain data are plotted in Fig. 9. However, due to the nature of dynamic testing, two caveats should be remembered. First, the curves are not necessarily representative of material behavior, as the specimens are not in equilibrium until near peak stress. Second, because the SHPB relies on wave propagation to determine stress and strain, post-peak results are unlikely to be useful. As shown previously (Fig. 7), specimens crack quickly, which alters their wave propagation characteristics. Also, the specimen may not be in contact with the bars after cracking. Thus, a large variety of post-peak behavior can be seen in Fig. 9. Three specimens (X-D-6B, X-D-11T, and Y-D-13T) were intact after testing and have stress-strain curves that show unloading following the maximum stress.

A plot of dynamic strength versus $\eta_\perp$ is given in Fig. 10. Specimens that were intact after testing are marked with an asterisk.
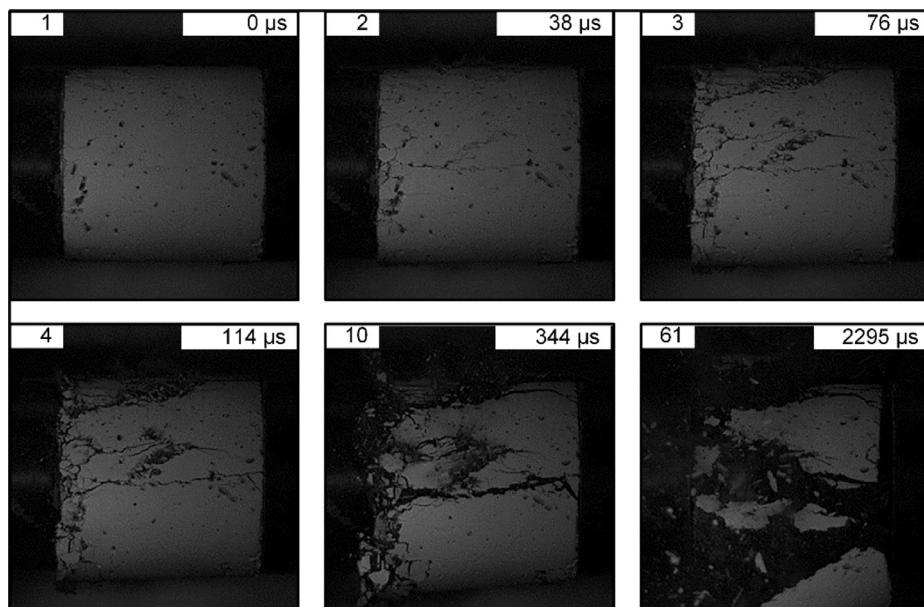

Fig. 7. Sequence of high-speed images showing failure of specimen Z-D-4T. The frame number is shown in the upper left, and the time relative to frame 1 is shown in the upper right.
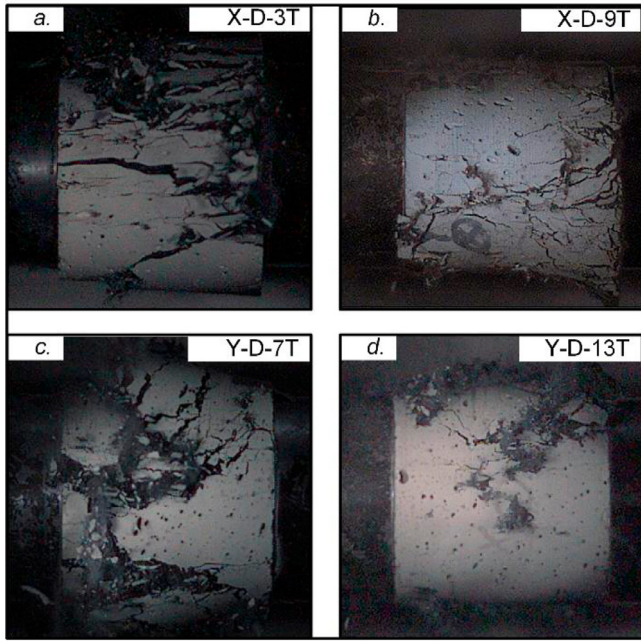
Fig. 8. High-speed images of fracture patterns: *a.* columnar, specimen X-D-3T; *b.* shear, specimen X-D-9T; *c.* cone-and-split, specimen Y-D-7T; *d.* side, specimen Y-D-13T.

Both cone-and-split and columnar fractures are characterized by vertical cracking, which the fibers can bridge effectively. In a shear fracture, cracking may occur in the same plane as fibers. These fibers have little or no crack-bridging ability because they are parallel to the crack.

Ductility under dynamic loading was assessed using the strain at peak stress, ε_o. A plot of ε_o as a function of $\eta_\perp$ is given in Fig. 11. Note that specimens that were intact after testing generally reached lower strains at peak stress. Despite some scatter, there is an overall trend of increasing ductility with $\eta_\perp$. When fibers are predominantly oriented perpendicular to the load, they are effective in bridging the cracks that form. This crack-bridging allows the specimen to reach a higher axial strain before fracture. A linear least-squares regression was performed to determine estimators for the slope (m) and intercept (b) in the linear function $\varepsilon_o = m\eta_\perp + b$. With all data points included, the fitted constants were $m = 0.0020$ and $b = 0.0106$. A hypothesis test was performed to determine whether the slope was significantly different from zero—that is, whether there was any trend in the data. A one-sample *t*-test resulted in $p = 0.038$ (df = 14, $t = 2.29$), indicating the slope was significantly different from zero at the $\alpha = 0.05$ level. Excluding the three specimens that did not completely fail during the test, the fitted constants were $m = 0.0018$ and $b = 0.0109$. A one-sample *t*-test resulted in $p = 0.035$ (df = 11, $t = 2.40$), again indicating the trend was significant at the $\alpha = 0.05$ level. The regression line shown in Fig. 11 was determined with the intact specimens excluded.

3.3. Experimental limitations

As mentioned before, several assumptions are typically made in analyzing SHPB data. One aspect of ensuring one-dimensional wave propagation is preparing specimens with flat and parallel ends. A tolerance of 0.5° was used, but not all specimens met this tolerance after end grinding. Therefore, the possible influence of deviation from parallel was investigated on results for dynamic compressive strength (Fig. 12) and dynamic compressive ductility (Fig. 13). For specimens with a deviation from parallel between 0.5 and 1°, the scatter in strength (Fig. 12) and ductility (Fig. 13) was comparable to the scatter for specimens that met the 0.5-degree tolerance. However, specimens with larger deviations from parallel had lower-
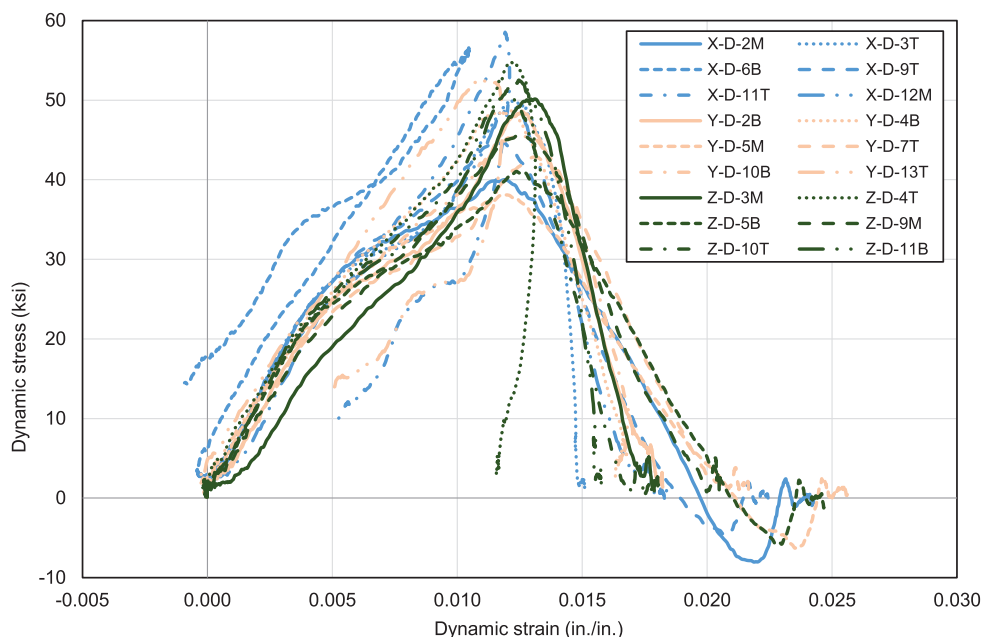
Interestingly, there is no clear trend in strength as a function of $\eta_\perp$. This may be related to the degree of alignment. The specimens in this study showed a realistic level of flow-induced preferential fiber orientation, but fibers were not perfectly aligned. Research on specimens in which all fibers are oriented in a given direction may yield more conclusive data. Nevertheless, some observations can be made from the current results. It seems that fiber orientation has no effect on the dynamic strength of Cor-Tuf Baseline. However, at a given orientation, the failure mode does affect the efficiency of the fiber reinforcement. For similar values of $\eta_\perp$, shear fractures occurred at lower stresses than columnar fractures. Cone-and-split fractures had strengths that were comparable to those from columnar fractures.

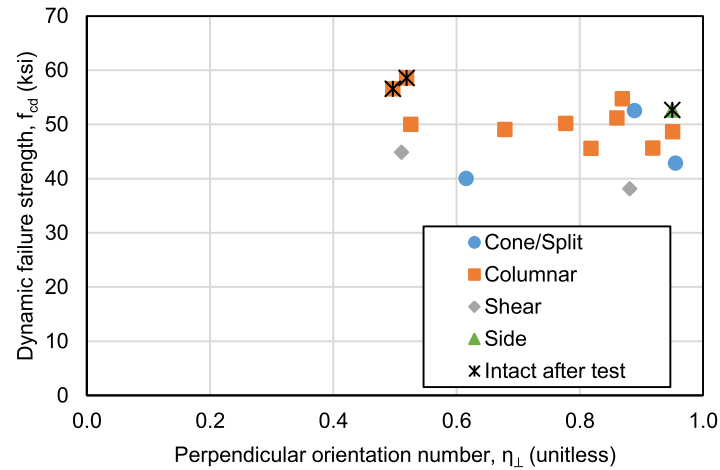**Fig. 9.** Dynamic stress-strain data for all specimens.

Fig. 10. Effect of the perpendicular orientation number on dynamic strength. The failure mode is indicated for each data point. Specimens that were intact after testing are marked with an asterisk.
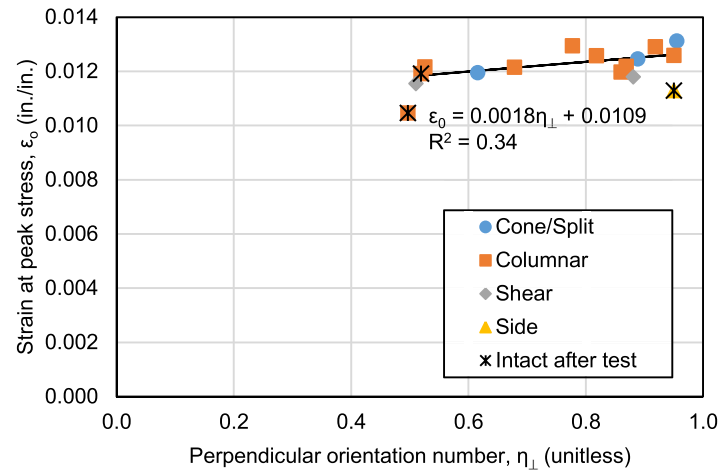

Fig. 11. Effect of the perpendicular orientation number on strain at peak stress. The failure mode is indicated for each data point. Specimens that were intact after testing are marked with an asterisk.

than-average strength. Strain at peak stress (Fig. 13) also increased for such specimens, indicating a lower stiffness, perhaps due to the irregular surface. Figs. 12 and 13 do not show a clear influence of deviation from parallel on strength and ductility in the present results. However, this does not indicate that parallel ends, in general, do not have an influence on results.

Although it is known that radial inertial confinement does contribute to the strength increase in SHPB compression tests of UHPC, the magnitude of the contribution is difficult to quantify. The linear elastic analysis performed by Forrestal et al. [12] could be used as an approximation, particularly for early times in the test, but it breaks down once the specimen begins to crush or crack. Because of the
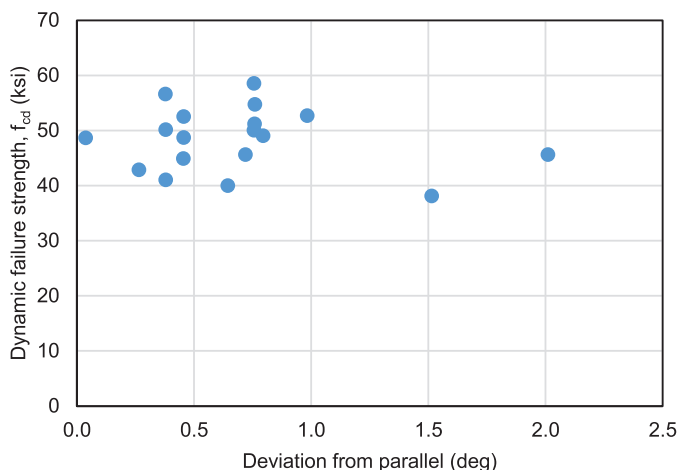

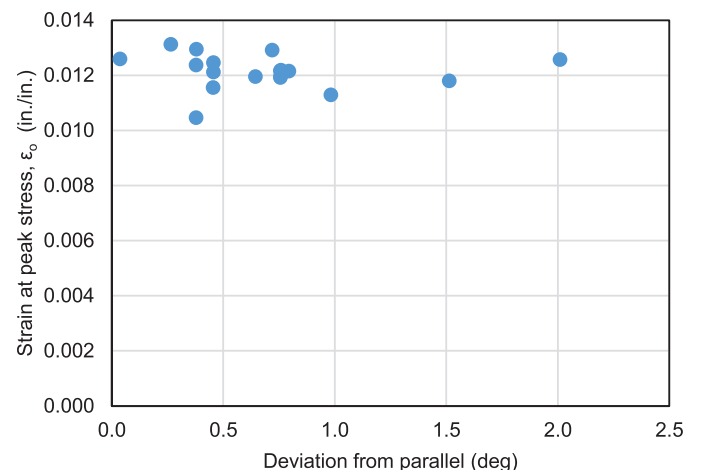**Fig. 12.** Dynamic compressive strength versus end deviation from parallel.

Fig. 13. Dynamic compressive ductility versus end deviation from parallel.

uncertainty associated with determining inertial confinement, no attempt is made to assess inertial confinement effects experimentally in the current work.

It is desirable for specimens to be in stress equilibrium so that test results are valid material properties. Because loads are applied extremely rapidly, it is unlikely that perfect stress equilibrium can be reached. However, Ravichandran and Subhash [34] have suggested an approximate condition for equilibrium. This condition and an analysis of its application to the test results are given in the Appendix. Based on the analysis, 12 of the specimens are known to have reached equilibrium prior to peak stress. As many as 16 specimens may have reached equilibrium, though differences between the strain gage channels make this hard to determine with certainty. In the worst case, the difference in stress between the specimen ends was 18% of the average stress in the specimen.

In this study, it was difficult to see the effects of fiber orientation clearly. There are likely two reasons for this. First, failure in compression occurs by different cracking patterns. In tension, cracks typically form perpendicular to the applied load, making orientation effects easier to study. The fracture patterns that occur are influenced by the presence of voids and other defects in addition to the distribution of fibers in the specimen. Second, while fiber orientation was statistically different for x-, y-, and z-direction specimens, the fibers were not unidirectionally aligned. This study focused on alignment due to flow in a typical structure. More sophisticated techniques to produce concrete with aligned fibers may be necessary for further study of orientation effects.

4. Conclusions

Preferential fiber orientation, such as that occurring in typical construction practice, has been investigated to determine its effect on dynamic strength and ductility of a UHPC. X-ray CT was used to determine fiber orientation in cores taken from a cast beam. CT scans showed that fibers were preferentially oriented in the direction of flow during casting, though fibers were not unidirectionally aligned. High strain rate compression tests with an SHPB indicated that, for the fiber orientations encountered, strength was independent of the perpendicular orientation number. Ductility, measured by the strain at peak stress, did increase with the perpendicular orientation number.

Appendix. Stress equilibrium

The stresses σ_1 and σ_2 at the input and output bar ends of the specimen, respectively, are given by Chen and Song [7]:

$$\sigma_1 = \frac{A_b E_b}{A_s}(\varepsilon_I(t) + \varepsilon_R(t)), \tag{A.1}$$

$$\sigma_2 = \frac{A_b E_b}{A_s}\varepsilon_T(t). \tag{A.2}$$

The relative stress difference, $R(t)$, used by Ravichandran and Subhash [34] is defined as

$$R(t) = \left|\frac{\Delta\sigma}{\sigma_m}\right| = 2\left|\frac{\sigma_1 - \sigma_2}{\sigma_1 + \sigma_2}\right| \tag{A.3}$$

where $\Delta\sigma$ is the stress difference between the specimen ends and σ_m is the mean stress. When $R(t) \leq 0.05$, the specimen is assumed to be in equilibrium [34].

In analyzing stress equilibrium in these tests, data from the A/B and C/D channels were used separately to avoid obscuring any discrepancies in results. For each specimen, the time of equilibrium, which is the first time t_e such that $R(t_e) \leq 0.05$, and the time of peak stress, t_p, were determined. Times were counted relative to the start of loading, which was defined as the first positive strain rate not immediately followed by a fluctuation back into negative values. This was used as an unambiguous method to identify the beginning of the loading pulse across multiple tests. Times to equilibrium and peak stress are given in Table A.1. The criterion $t_e < t_p$ was used to

Table A.1
Analysis of time to stress equilibrium for the two strain gage channels.

Specimen ID	Time to equilibrium, t_e (μs)		Time to peak stress, t_p (μs)		Relative stress difference at peak stress, $R(t_p)$	
	A/B	C/D	A/B	C/D	A/B	C/D
X-D-2M	121	117	131	121	0.123	0.038
Y-D-2B	137	132	142	138	0.054	0.063
X-D-3T	134	126	135	139	0.040	0.124
Z-D-3M	133	129	139	142	0.014	0.128
Z-D-4T[a]	141	131	**139**	137	0.084	0.040
Y-D-4B	132	124	137	124	0.020	0.046
Y-D-5M[a]	126	112	**125**	114	0.054	0.014
Z-D-5B[a]	129	115	**128**	120	0.064	0.041
X-D-6B[a]	146	144	**143**	136	0.086	0.146
Y-D-7T	128	123	134	132	0.060	0.179
X-D-9T	131	118	131	123	0.030	0.112
Z-D-9M	128	123	133	132	0.055	0.161
Z-D-10T	133	120	137	128	0.023	0.136
Y-D-10B[a]	136	124	**135**	129	0.077	0.080
X-D-11T	141	134	148	142	0.018	0.044
Z-D-11B	136	135	138	138	0.003	0.024
X-D-12M	147	139	154	145	0.100	0.053
Y-D-13T[a]	138	137	**128**	**130**	0.170	0.142
Mean	134	127	137	132	0.060	0.087
St. Dev.	7	9	7	9	0.043	0.053
COV	5%	7%	5%	7%	71%	61%

[a] Peak stress occurred before equilibrium for the bolded channel.

determine if stress equilibrium was reached. Note that $R(t_p)$ is not necessarily a useful indicator for equilibrium. If the specimen has already begun to fail, it may not be in stress equilibrium at peak stress, even if it was prior to t_p.

References

[1] Laranjeira F, Aguado A, Molins C, Grünewald S, Walraven J, Cavalaro S. Framework to predict the orientation of fibers in FRC: a novel philosophy. Cem Concr Res 2012;42(6):752–68. https://doi.org/10.1016/j.cemconres.2012.02.013.

[2] Mansur MA, Chin MS, Wee TH. Stress-strain relationship of high-strength fiber concrete in compression. J Mater Civil Eng 1999;11(1):21–9.

[3] Leonhardt S, Lowke D, Gehlen C. Effect of fibres on impact resistance of ultra high performance concrete. In: Proceedings of the 3rd international symposium on UHPC and nanotechnology for high performance construction materials. Kassel, Germany. Kassel University Press; 2012. p. 811–7.

[4] VanSlembrouck DJ. Compression behavior at high strain rate for an ultra high performance concrete. MS thesis. Houghton, MI: Michigan Technological University; 2015.

[5] Kolsky H. An investigation of the mechanical properties of materials at very high rates of loading. Proc Phys Soc B 1949;62(11):676–700. https://doi.org/10.1088/0370-1301/62/11/302.

[6] Frew DJ, Forrestal MJ, Chen W. Pulse shaping techniques for testing brittle materials with a split Hopkinson pressure bar. Exp Mech 2002;42(1):93–106. https://doi.org/10.1007/bf02411056.

[7] Chen W, Song B. Split hopkinson (Kolsky) bar: design, testing and applications. New York: Springer; 2011. https://doi.org/10.1007/978-1-4419-7982-7.

[8] Williams EM, Graham SS, Reed PA, Rushing TS. Laboratory characterization of cor-tuf concrete with and without steel fibers. Vicksburg, MS: U.S. Army Engineer Research and Development Center; 2009 Technical report ERDC/GSL TR-09-22.

[9] Mondal AB. Dynamic triaxial compression experiments on cor-tuf specimens. MS thesis. West Lafayette, IN: Purdue University; 2012.

[10] Li QM, Meng H. About the dynamic strength enhancement of concrete-like materials in a split Hopkinson pressure bar test. Int J Solids Struct 2003;40(2):343–60. https://doi.org/10.1016/s0020-7683(02)00526-7.

[11] Zhang M, Wu H, Li Q, Huang F. Further investigation on the dynamic compressive strength enhancement of concrete-like materials based on split Hopkinson pressure bar tests. Part I: experiments. Int J Impact Eng 2009;36(12):1327–34. https://doi.org/10.1016/j.ijimpeng.2009.04.009.

[12] Forrestal MJ, Wright TW, Chen W. The effect of radial inertia on brittle samples during the split Hopkinson pressure bar test. Int J Impact Eng 2007;34(3):405–11. https://doi.org/10.1016/j.ijimpeng.2005.12.001.

[13] Hao Y, Hao H, Li Z-X. Numerical analysis of lateral inertial confinement effects on impact test of concrete compressive material properties. Int J Protect Struct 2010;1(1):145–67. https://doi.org/10.1260/2041-4196.1.1.145.

[14] Kim DJ, Sirijaroonchai K, El-Tawil S, Naaman AE. Numerical simulation of the Split Hopkinson Pressure Bar test technique for concrete under compression. Int J Impact Eng 2010;37:141–9. https://doi.org/10.1016/j.ijimpeng.2009.06.012.

[15] Mu ZC, Dancygier AN, Zhang W, Yankelevsky DZ. Revisiting the dynamic compressive behavior of concrete-like materials. Int J Impact Eng 2012;49:91–102. https://doi.org/10.1016/j.ijimpeng.2012.05.002.

[16] Krenchel H. Fibre reinforcement: theoretical and practical investigations of the elasticity and strength of fibre-reinforced materials. Copenhagen: Akademisk Forlag; 1964.

[17] Krenchel H. Fibre spacing and specific fibre surface. In: Neville A, editor. Fibre reinforced cement and concrete. UK: The Construction Press; 1975. p. 69–79.

[18] Gettu R, Gardner DR, Saldivar H, Barragán BE. Study of the distribution and orientation of fibers in SFRC specimens. Mater Struct 2005;38(1):31–7. https://doi.org/10.1007/bf02480572.

[19] Lee Y, Lee S, Youn J, Chung K, Kang T. Characterization of fiber orientation in short fiber reinforced composites with an image processing technique. Mater Res Innov 2002;6(2):65–72. https://doi.org/10.1007/s10019-002-0180-8.

[20] Eik M, Lõhmus K, Tigasson M, Listak M, Puttonen J, Herrmann H. DC-conductivity testing combined with photometry for measuring fibre orientations in SFRC. J Mater Sci 2013;48(10):3745–59. https://doi.org/10.1007/s10853-013-7174-3.

[21] Woo LY, Wansom S, Ozyurt N, Mu B, Shah SP, Mason TO. Characterizing fiber dispersion in cement composites using AC-Impedance Spectroscopy. Cem Concr Comp 2005;27(6):627–36. https://doi.org/10.1016/j.cemconcomp.2004.06.003.

[22] Karhunen K, Seppänen A, Lehikoinen A, Monteiro PJM, Kaipio JP. Electrical resistance tomography imaging of concrete. Cem Concr Res 2010;40(1):137–45. https://doi.org/10.1016/j.cemconres.2009.08.023.

[23] Barnett SJ, Lataste J-F, Parry T, Millard SG, Soutsos MN. Assessment of fibre orientation in ultra high performance fibre reinforced concrete and its effect on flexural strength. Mater Struct 2010;43(7):1009–23. https://doi.org/10.1617/s11527-009-9562-3.

[24] Landis EN, Keane DT. X-ray microtomography. Mater Charact 2010;61(12):1305–16. https://doi.org/10.1016/j.matchar.2010.09.012.

[25] Radon J. Über die Bestimmung von Funktionen durch ihre Integralwerte längs gewisser Mannigfal-ligkeiten. Ber Verh Sächs Akad Wiss 1917;69:262–77.

[26] Scott DA, Long WR, Moser RD, Green BH, O'Daniel JL, Williams BA. Impact of steel fiber size and shape on the mechanical properties of ultra-high performance concrete. Vicksburg, MS: U.S. Army Engineer Research and Development Center; 2015. Technical report ERDC/GSL TR-15-22.

[27] Trainor KJ, Foust BW, Landis EN. Measurement of energy dissipation mechanisms in fracture of fiber-reinforced ultrahigh-strength cement-based composites. J Eng Mech 2013;139(7):771–9. https://doi.org/10.1061/(asce)em.1943-7889.0000545.

[28] Oesch TS. Investigation of fiber and cracking behavior for conventional and ultra-high performance concretes using x-ray computed tomography. Champaign, IL: University of Illinois at Urbana-Champaign; 2015.

[29] Groeneveld AB. Effect of fiber orientation on dynamic compressive properties of an ultra-high performance concrete. MS thesis. Houghton, MI: Michigan Technological University; 2016.

[30] Gilbertson CG. Dynamic properties of wood using the split-Hopkinson pressure bar. Houghton, MI: Michigan Technological University; 2011.

[31] Games PA, Howell JF. Pairwise multiple comparison procedures with unequal n's and/or variances: a Monte Carlo study. J Educ Behav Stat 1976;1(2):113–25. https://doi.org/10.2307/1164979.

[32] Minitab, Inc. Minitab 17 Statistical Software. 2010.

[33] ASTM. ASTM C39/C39M, standard test method for compressive strength of cylindrical concrete specimens. West Conshohocken, PA: ASTM International; 2015. https://doi.org/10.1520/c0039_c0039m-15.

[34] Ravichandran G, Subhash G. Critical appraisal of limiting strain rates for compression testing of ceramics in a split Hopkinson pressure bar. J Am Ceram Soc 1994;77(1):263–7. https://doi.org/10.1111/j.1151-2916.1994.tb06987.x.